THE UNIVERSITY OF CHICAGO

AZIMUTHAL ASYMMETRIES AND VIBRATIONAL MODES IN BUBBLE

PINCH-OFF

A DISSERTATION SUBMITTED TO

THE FACULTY OF THE DIVISION OF THE PHYSICAL SCIENCES

IN CANDIDACY FOR THE DEGREE OF

DOCTOR OF PHILOSOPHY

DEPARTMENT OF PHYSICS

BY

LAURA E. SCHMIDT

CHICAGO, ILLINOIS

DECEMBER 2008

ABSTRACT

The pressure-driven inertial collapse of a cylindrical void in an inviscid liquid is an integrable, Hamiltonian system that forms a finite-time singularity as the radius of the void collapses to zero. Here it is shown that when the natural cylindrical symmetry of the void is perturbed azimuthally, the perturbation modes neither grow nor decay, but instead cause constant amplitude vibrations about the leading-order symmetric collapse. Though the amplitudes are frozen in time, they grow relative to the mean radius which is collapsing to zero, eventually overtaking the leading-order symmetric implosion. Including weak viscous dissipation destroys the integrability of the underlying symmetric implosion, and the effect on the stability spectrum is that short-wavelength disturbances are now erased as the implosion proceeds. Introducing a weak rotational flow component to the symmetric implosion dynamics causes the vibrating shapes to spin as the mean radius collapses. The above theoretical scenario is compared to a closely related experimental realization of void implosion: the disconnection of an air bubble from an underwater nozzle. There, the thin neck connecting the bubble to the nozzle implodes primarily radially inward and disconnects. Recent experiments were able to induce vibrations of the neck shape by releasing the bubble from a slot-shaped nozzle. The frequency and amplitude of the observed vibrations are consistent with the theoretical prediction once surface tension effects are taken into account.

ACKNOWLEDGMENTS

TABLE OF CONTENTS

LIST OF FIGURES

CHAPTER 1

INTRODUCTION

One of the most fundamental questions in fluid mechanics, is how does a volume of fluid break into two? It happens all the time, all around us – for example a stream of water falling from a faucet breaks into droplets, then these droplets splash as they hit the sink, sending off even more tiny satellite droplets. Despite the ubiquitous nature of the phenomena, we still do not have a complete understanding of the process for a generic combination of fluids [1, 2]. The question is even more interesting because when a fluid undergoes a topological transition, a singularity occurs in the governing Navier-Stokes equations, where physical quantities such as the liquid pressure or velocity diverge in a finite time [3, 4, 5]. The mathematical appeal of singularity formation and technological relevance of the generation of droplets and bubbles has spurred much interest in topological changes of fluid surfaces in past years. Many of the theoretical works have concentrated on characterizing the universal features of the approach to the singularity [6, 7, 8].

However, recent results from multiple experimental groups have indicated that the pressure-driven implosion of a gas cavity in an inviscid liquid is *not* universal and that small asymmetries present in the initial state are preserved. The retention of such disturbances has the potential to dramatically alter the final state at breakup. In these experiments, a cavity is created and then disconnected either by quasi-statically releasing a bubble from a nozzle submerged in a liquid (see Fig. 1.1) [9, 10, 11, 12, 13], by impacting a solid disc into a liquid bath [14, 15, 16], or by placing a bubble in a co-flowing stream [17]. The cavity forms following the bubble as it rises, following the disc as it passes into the bath, or in the middle of the bubble as it is pulled apart by the divergent flow. For all cases, the final dynamics before disconnection is

dominated by a rapid inertia-driven implosion, not by surface tension which drives the breakup of a liquid drop in air [6, 18, 19]. In the only detailed investigation of the effect of initial azimuthal asymmetry on the bubble pinch-off dynamics Keim *et al* [10] found that tilting the nozzle by $2°$ results in side-by-side satellite bubble formation and non-circular neck cross sections. Tilts of even less than a tenth of a degree result in visibly asymmetric neck profiles, demonstrating that the generic form of pinch-off realized in experiments is asymmetric. Despite the fact that azimuthal asymmetry is usually observed in the experiments, it has only recently begun to be explored theoretically [13].

The inertial implosion of a gas cavity belongs to a different class of dynamics which are not universal, but instead have a precise memory of the details of the initial state. To understand the origin of the observed memory, consider a theoretically simpler but closely related system – the implosion of a cylindrical void in an inviscid liquid. Integrable systems such as this have a perfect memory (with as many conserved quantities as independent variables), and when they are perturbed, the Kolmogorov-Arnold-Moser theorem predicts that the dynamics will have trajectories which, for the most part, closely follow those of the original integrable dynamics [20]. In this system, which is both integrable and singular, the underlying memory manifests itself in a particularly simple way – as the amplitudes of shape disturbances become frozen in time as the cavity implodes [13]. The constant-amplitude disturbances cause vibrations of the void's cross section shape as the implosion proceeds, with frequencies proportional to $1/\tau$, where τ is the time until the radius closes to zero. Since the frequency diverges as $\tau \to 0$, the shapes chirp, vibrating faster and faster as the void closes. This presents a natural explanation why the experiments observe a variety of disconnection scenarios depending on the specific experimental conditions. Since the experiments have a dynamics close to an integrable dynamics, small perturbations

are retained as the hole closes.

The first purpose of this paper is to investigate additional physical effects which are mathematically interesting and experimentally relevant. Including weak viscous dissipation in the model destroys the integrability of the leading order implosion dynamics, and including a non-zero circulation to the liquid flow prevents the formation of a singularity. Both effects have consequences on how a disturbance on the void surface evolves over time, but within the experimentally accessible regime and for large wavelength (small mode number) disturbances do not qualitatively change the freezing and chirping behavior. The second purpose is to directly connect the theoretical model to the experimental realization for both the symmetric and perturbed cases. This requires including surface tension, which, though it becomes asymptotically irrelevant compared to inertial forces, has lingering effects on the vibration frequency within the experimental regime.

We begin by reviewing the cylindrically symmetric implosion dynamics and demonstrate that the dynamics can be recast into Hamiltonian form. We examine the model's implications for quasi-2D (nearly cylindrical) void collapse and show that though the integrable dynamics is fundamentally *non*-universal, it appears self-similar in this limit. Then we consider the stability of the cylindrically symmetric implosion when subjected to azimuthal shape perturbations and derive the mode amplitude freezing and chirping behavior, including asymptotic logarithmic corrections. Next, we investigate changes to the leading-order symmetric dynamics and vibrational mode behavior after taking into account viscous dissipation and introducing a rotational flow. Finally, we discuss the relation between experiments for the cylindrically symmetric and azimuthally perturbed cases, ending with a direct comparison between the theoretical prediction for a single vibrational mode and an experimentally induced vibration in the neck of a bubble released from an oblong nozzle.
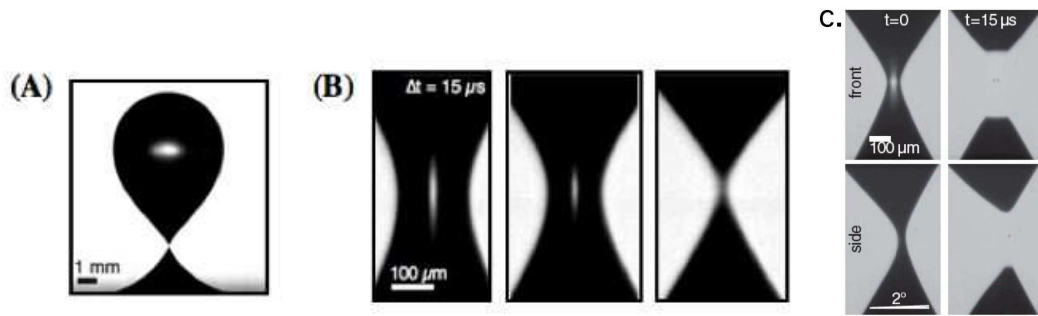
Figure 1.1: A. Air bubble released from underwater nozzle, images from N. Keim (U. Chicago) B. Close-up images of radial implosion of neck as it disconnects. C. Nozzle is tilted by two degrees and shapes before and after disconnection show signs of the asymmetry. Two tiny side-by-side satellite bubbles are left behind, evidence of the inherent memory in this system. Nozzle is tilted towards viewer in the 'front' view, and to the left side in the 'side' view.

CHAPTER 2

AXISYMMETRIC CAVITY IMPLOSION

The implosion of an arbitrarily shaped cavity is a very complicated, fully 3D problem. However, with additional geometric constraints the problem is simplified. The dynamics of a spherical cavity have been studied for over a century [21, 22, 23], and is an integral component in the understanding cavitation [24] and the phenomena of sonoluminescence [25]. The inertial collapse of a cylindrical cavity was first studied in relation to bubble production from underwater nozzles [26, 27] and has more recently been applied to cavity collapse in liquids after solid body impact [14] and cavities in granular media [28]. The inner gas dynamics can also play a role in the asymptotic dynamics [29]. Here, we briefly reexamine the cylindrically symmetric implosion and its implications so that we can later characterize its stability when perturbed azimuthally.

The problem under consideration is the inertial implosion of an infinite cylindrical vacuum cavity in an inviscid liquid. After the void is created it begins to implode inwards because the pressure inside the void is less than the pressure of the liquid outside. The inviscid fluid flow is governed by Euler equations: $\partial \vec{u}/\partial t + \vec{u} \cdot \vec{\nabla} \vec{u} = -\vec{\nabla} P/\rho$), where $\vec{u}$ is the local velocity field, P the pressure, and ρ the liquid density. When incompressible, the continuity equation for volume conservation $\vec{\nabla} \cdot \vec{u} = 0$ applies. If the process starts from rest, the flow must also be irrotational ($\vec{\nabla} \times \vec{u} = 0$) for all times and thus we can also write the velocity as $\vec{u} = \vec{\nabla} \Phi$ where Φ is the velocity potential which satisfies Laplace's equation $\vec{\nabla}^2 \Phi = 0$, following from the continuity equation. Solving for the flow is just a matter of solving Laplace's equation, which is linear and time-independent. The difficulty in this problem arises via the non-linear dynamic boundary conditions (the normal stress balance on the interface) which

determines how the interface moves over time.

To describe the implosion of the cylindrical cavity, we naturally use circular cylindrical coordinates, with the z-axis aligned along the axis of the cylinder, and the surface at $r = R(t)$. The implosion dynamics is completely z-independent, and two-dimensional because we can consider the implosion of a circle of radius $R(t)$ in a sheet of water. If no rotational flow u_θ is present, the solution from the Euler equations for the flow field is purely a convergent radial flow of the form $u_r(r, t) = -Q(t)/r$ and velocity potential $\Phi = -Q(t) \ln(r)$. This corresponds to the flow of a point-sink with strength $Q(t)$, which will be determined by the boundary conditions. The strength $Q(t)$ is related to the areal flux of incoming water by $\mathrm{d}A/\mathrm{d}t = 2\pi R\dot{R} = 2\pi Q(t)$. The first boundary condition on the motion of the interface is the kinematic condition that the interface moves with a velocity equal to that of the normal velocity of the liquid at the interface:

$$u_r(r, t)|_{R(t)} = -\frac{Q(t)}{R} = \dot{R}, \tag{2.1}$$

showing that the flux $Q(t) = -R\dot{R}$ and the velocity field at any point in time are completely determined by the radius of the hole and it's velocity, $u_r(r, t) = R\dot{R}/r$.

To find the evolution of the radius $R(t)$, Euler's equations can be integrated over the region of the liquid (from $r = R(t)$ to R_∞) where R_∞ is a far away distance where the radial flow has decayed or where the inner flow transitions to an outer flow of a different form. In 2D we must impose this length scale to keep the energy finite because the potential does not decay as $r \to \infty$. Experimentally, this scale will depend on the system size and set-up. Integrating Euler's equations yields the Bernoulli integral [23] for the pressure in the liquid $P(r, t)$. It essentially constitutes

a conservation of energy for each fluid volume. In this case it yields

$$P(r,t) = P_\infty + \rho \left(\frac{\partial \Phi}{\partial t} + \frac{1}{2}|\nabla\Phi|^2 \right)\Bigg|_r^{R_\infty}, \tag{2.2}$$

where P_∞ is the pressure at R_∞ taken as constant. The normal stress balance at the imploding surface is given by Laplace's formula for the pressure jump across the interface $P(R,t) = P_0 - \gamma\kappa$, where P_0 is the cavity pressure taken as constant, γ is the line tension (analog of surface tension in 2D), and κ is the curvature which is $1/R(t)$ for a circle. By evaluating the pressure in (2.2) at the surface, we can eliminate it via the normal stress balance and derive an evolution equation for the radius $R(t)$:

$$\Delta P + \frac{\gamma}{R(t)} = -\rho \left(\frac{\partial \Phi}{\partial t} + \frac{1}{2}|\nabla\Phi|^2 \right)\Bigg|_{R(t)}^{R_\infty}. \tag{2.3}$$

In (2.3) we have incorporated the fact that the pressure P_∞ is higher than P_0 by an amount ΔP. Ignoring the terms in (2.3) which are $O(R/R_\infty)$ or smaller and inserting the known form for $\Phi(t)$ yields the well known 2-D analog of the Rayleigh-Plesset equation

$$\Delta P + \frac{\gamma}{R} = \frac{\rho}{2}\dot{R}^2 - \rho(\dot{R}^2 + R\ddot{R})\ln(R_\infty/R), \tag{2.4}$$

where the dot denotes a time derivative [24].

Equation (2.4) is the second-order non-linear ordinary differential equation which determines the evolution of the radius $R(t)$ as it collapses to zero. Any one dimensional ordinary differential equation of the form $(\ddot{q} + f(q)\dot{q}^2 + g(q) = 0)$, like (2.4) above, can be integrated and recast as a Hamiltonian [30]. We are not surprised by this because in fact any free boundary problem with inviscid, irrotational, and incompressible flow is Hamiltonian by nature [31]. However, whereas the Hamiltonian for an arbitrary flow may be quite complicated, here the Hamiltonian takes a particularly

simple form and represents the total energy per unit length of the system. The fact that the dynamical equation (2.4) can be integrated has been remarked before [12, 14] but the implications of the integrability had not been fully exploited in this context. The integrability of the leading order dynamics combined with the approach to a singularity (where external length and time-scales are irrelevant) is the origin of the unusual flat mode amplitude stability spectrum observed in this system [13] and other focusing phenomena like spherical void collapse [24] or cylindrical [32] and spherical shock wave implosion [33].

The total energy is the sum of the kinetic energy of the water in motion and the potential energy associated with opening up the hole in the liquid:

$$H(R, P_R) = E = \frac{P_R^2}{2M(R)} + \Delta P \pi R^2 + \gamma \, 2\pi R, \qquad (2.5)$$

where R is the void radius, $P_R = M(R)\mathrm{d}R/\mathrm{d}t$ is the radial momentum of the implosion, $M(R) = 2\rho\pi R^2 \ln(R_\infty/R)$ is the mass of liquid in motion. The Hamiltonian is conserved and thus the total implosion energy E is a constant. The kinetic term is simply the total kinetic energy of the sheet of water in motion:

$$K.E. = \rho \int_R^{R_\infty} u_r^2 \, r dr d\theta = \frac{1}{2} M(R)\dot{R}^2 = \frac{P_R^2}{2M(R)}. \qquad (2.6)$$

The potential energy due to the pressure $\Delta P \pi R^2$ comes from the work that must be done against the external pressure to form the hole and the surface energy $\gamma 2\pi R$ is the energy cost for adding surface length to the hole. One can easily check that this formulation is equivalent to the 2-D Rayleigh-Plesset equation (2.4) by applying Hamilton's equations of motion ($\dot{R} = \partial H/\partial P_R$, $\dot{P}_R = -\partial H/\partial R$). One technical advantage of using the equation in Hamiltonian, or integrated form, is that now we

no longer need to solve a 2nd order ODE for $R(t)$, but can simply integrate the equation for dR/dt, which in fact has known solutions [12, 14]. A more fundamental implication is that it is now clear that this system belongs to the class of integrable dynamics as it has one degree of freedom and one conserved quantity, the energy.

2.1 Asymptotic energy balance and closure dynamics

For a void which starts from rest, initially the energy is due completely to the potential contributions from the overpressure in the liquid and surface tension. From (2.5) we can see that as the void closes, $R \to 0$, this energy is transferred into kinetic energy. The asymptotic energy balance is

$$E = \frac{1}{2}M(R)\dot{R}^2 = \pi\rho \ln(R_\infty/R)(R\dot{R})^2. \tag{2.7}$$

A singularity occurs because the closure rate $\dot{R}$ must diverge to compensate for the decreasing area of the void in order to maintain constant energy. Another way to say this is that since the mass of liquid in motion $M(R)$ decreases to 0 at the moment of disconnection, the closure rate $\dot{R}$ must diverge. Both surface tension and the pressure effects thus become negligible relative to inertia as the implosion proceeds and $\dot{R}$ diverges.

The leading order dynamics in the inertially dominated regime can be found by examining the right hand side of (2.4) or equivalently the energy balance in Eq. (2.7). From the energy balance, we see that the areal flux $Q = -R\dot{R} = \sqrt{E/\pi\rho \ln(R_\infty/R)}$ is slowly varying as $R \to 0$. The flux slowly approaches zero as less and less liquid is required to move in to fill the hole. Approximating the flux Q as constant, yields the power law scaling $R = \alpha(t_b - t)^{1/2}$ first proposed by Longuet-Higgins *et al* in

a study of the sound emission from bubbles released underwater [26]. Here, t_b is the closure time, and α is related to the flux Q by $\alpha^2 = 2Q$ with dimensions of diffusivity (length^2/time). The prefactor α depends on the experimental specifics. For a bubble released from an underwater nozzle the appropriate physical scaling is $\alpha^2 \sim \sqrt{\gamma R_N/\rho}$, with R_N the nozzle radius [10].

In (2.4) if we include the logarithmic term but treat it as nearly constant, we find an acceptable power law solution $R(t) = \alpha(t_b - t)^\beta$, with a weakly varying apparent exponent,

$$\beta = \frac{1}{2} \cdot \frac{1}{1 - \frac{1}{4\ln(R_\infty/R)}}. \tag{2.8}$$

The exponent β tends towards $1/2$ very slowly as $R \to 0$, but remains slightly greater than $1/2$, consistent with experimental observations of exponents in the range $0.54 - 0.57$ [9, 14, 10, 11]. This is a refinement of the first estimate of power law of $\beta = 1/2$ from [26] to include the weak logarithmic dependence on R, consistent with previous analyses [14, 29].

2.2   Axial variation

The above analysis is for the radial implosion of a perfectly cylindrical void, or equivalently, the implosion of a circular void in a 2D sheet of inviscid liquid. To extend the results to make predictions about how the full profile of 3D cavity (like the nearly cylindrical neck connecting an air bubble to an underwater nozzle) collapses we make a long-wavelength approximation for the neck radius so that the variation in the radius satisfies $\mathrm{d}R/\mathrm{d}z \ll 1$. This approximation was first used in [26] with the leading order dynamics treated as quasi-2D, and follows the above analysis for a cylinder but with z simply treated as a parameter. The flow at each height converges radially with flux Q, and is isolated from any coupling in the z-direction (there is no energy

or momentum transfer along z). For simplicity, we first examine the result ignoring logarithmic corrections so that the flux is constant in time (corresponding to the $R = \alpha \tau^{1/2}$ power law) and in z.

We initialize the surface at some $t = 0$ within the inertially dominated implosion regime. In the region near the neck minimum the shape is quadratic

$$R(z, t = 0) = H(z) = H_0 + c_0 z^2. \tag{2.9}$$

To stay within the quasi-2D limit the aspect ratio is constrained to be small, $H_0/L = \sqrt{c_0 H_0} \ll 1$, where we have used the axial length scale $L = \sqrt{H_0/c_0}$. Taking the approximation that the flux is constant, we can write the evolution of the profile as

$$R(z, t) = \alpha(t_b(z) - t)^{1/2}, \tag{2.10}$$

with the only difference between the evolution of the radius at difference heights being the implosion time, $t_b(z)$, which is set by the initial radius profile.The implosion time is the time when the radius at that height will collapse to zero as determined by the initial size (2.9):

$$t_b(z) = \left(\frac{H(z)}{\alpha}\right)^2. \tag{2.11}$$

With nothing to break the up/down symmetry about $z = 0$, the height which starts with the minimum radius H_0, will be the height of the disconnection event at $t = t_* = t_b(0)$. Writing the shape evolution in terms of the time until disconnection $\tau = t_* - t$ yields

$$R(z, \tau) = \alpha \left(\left(\frac{H(z)}{\alpha}\right)^2 - \left(\frac{H(0)}{\alpha}\right)^2 + \tau\right)^2. \tag{2.12}$$

By proper rescaling of the axial and radial coordinates, the evolution has a self-similar

form. Taking $\zeta = R/h_{min}$ and $\eta = z/h_{min}$ with $h_{min} = R(z = 0, t)$, the shape in the rescaled coordinates is approximated by:

$$\zeta = (2c_0 H_0 \eta^2 + 1)^{1/2}. \tag{2.13}$$

In the limit $h_{min} \to 0$, the shapes becomes conical ($R(z) = \sqrt{2c_0 H_0}\, z$) as seen in the experiments (Fig. 1.1) and shown in [26]. The relevant axial length scale is proportional to h_{min}, so that it decreases in pace with the radial scale and the aspect ratio of the shapes are maintained. Of importance is the dependence of the self-similar form on the initial aspect ratio $\sqrt{c_0 H_0}$. The final slope of the cones is directly dependent on the initial aspect ratio of the quadratic neck shape. An initially slender shape will remain slender and the long-wavelength approximation analysis is self-consistent in this respect.

Accounting for the logarithmic corrections to the power law exponent β in Eq. 2.8, we find a self-similar form

$$\zeta = (b\eta^2 + 1)^\beta, \tag{2.14}$$

with $\eta = z/h_{min}^{1/2\beta}$ and $b = c_0 H_0^{1/\beta - 1}/\beta$. The region where the shape is approximated by this form is bounded by

$$\eta \ll \sqrt{\frac{H_0}{c_0(\frac{1}{\beta} - 1)h_{min}^{1/\beta}}}, \tag{2.15}$$

which grows as h_{min} shrinks to 0. This form assumes that nearby layers evolve with the same α and β, a good approximation for slowly varying shapes because α and β themselves have only logarithmic dependencies on the local radius $R(z, t)$. Accounting for the weak z-variation of α and β, and solving the governing equations self-consistently replacing R_∞ with the axial length scale yields slight corrections to

the exponent [8].

Now, with the logarithmic corrections included, the axial length scale is proportional to $h_{min}^{1/2\beta}$ which decreases almost in pace, but a bit slower, than the radial scale. For a power law measured over a finite range of time we can write $h_{min} \propto \tau^{1/2+\delta}$ so that the axial scale $\propto \tau^{1/2-\delta}$, where δ measures the difference in the exponent from $1/2$, $\delta = 1/4 \ln(R_\infty/h_{min})$. In other words, if the radius is decreasing with a power slightly greater than $1/2$ (as observed in the experiments), then the quasi-2D model predicts the axial length scale will decrease with a power equally less than $1/2$. This result is qualitatively consistent with experimental measurements of the axial radius of curvature at the minimum [14, 11] which find powers less than but still close to $1/2$.

It is worthwhile to note that although the profiles have a self-similar form, it does not mean that the dynamics here is universal. Though often times universal dynamics exhibit self-similarity, in this case the reverse is not true. The underlying dynamics here is in fact nearly integrable, with the implosion energy at every height $E(z)$ conserved.

When extending the 2D-cylindrically symmetric model to capture the evolution of axisymmetric 3D shapes, we must also modify the Laplace pressure contribution due to surface tension at the interface which appears in the normal stress balance. Now, the surface is no longer a curve in a plane, but has an axial curvature component. Because the surface is curved outwards in the axial direction, it works in opposition to the azimuthal inwards curvature, effectively reducing the Laplace pressure jump across the interface. Directly from above, we know that the axial curvature at the minimum will increase at roughly the same rate as the radial curvature. This fact will later allow us to simply include the effect of the axial curvature by reducing the Laplace pressure by a fractional amount when comparing to the experiments over a

limited range. We can write the axial radius of curvature $R_{ax} = \chi h_{min}$, where χ is a constant determined by the initial aspect ratio from (2.13). Thus, a more realistic value of the Laplace pressure jump

$$\gamma\kappa = \gamma(1/h_{min} - 1/R_{ax}) = \gamma(1 - 1/\chi)/h_{min} \qquad (2.16)$$

can be used in (2.3).

The quasi-2D model outlined above provides a simple way to interpret and analyze the experimental results available today. It contains all the ingredients necessary to explain experimental observations of the time dependence of cavity profiles during implosion. We will see it is more than sufficient for the purposes of the present paper, not to predict the complete details of the asymptotic approach to the singularity, but to examine the effect of azimuthal asymmetry on the implosion dynamics within the experimental regime.

CHAPTER 3

AZIMUTHAL PERTURBATIONS

With the axisymmetric implosion dynamics in the limit of an infinite cylinder now determined by equation (2.4) or conservation of the Hamiltonian (2.5), we can begin to investigate the stability of the implosion under a slight azimuthal shape distortion which destroys the symmetry. Because the underlying leading order dynamics is integrable and possesses a natural memory mechanism via conservation of the energy, we will see the stability spectrum takes a special form. No single wavelength perturbation will grow fastest to overtake the others, as typically occurs in interfacial instabilities. Instead, all the modes will grow at the same rate, logarithmically slow relative to the rapid collapse of the mean radius. This unique property is the result of the combination of the approach towards a singularity and the integrable dynamics [13]. Since all modes grow identically, the initial spectrum of mode amplitudes for a generic distortion is frozen in time as the singularity is approached, encoding an infinite amount of information about the initial state in form of vibrational modes about the radial implosion.

Representing a distortion to the shape as the sum over the Fourier modes $\cos(n\theta)$ shifts the surface to lie at

$$r = S(\theta, t) = R(t) + \sum_n b_n(t) \ \cos(n\theta), \tag{3.1}$$

where the $b_n(t)$ are the mode amplitudes and assumed to be small relative to mean radius $R(t)$ $(b_n(t)/R(t) \ll 1)$. The velocity potential and velocity field in the liquid depend on the boundary conditions on the surface, so distorting the surface causes a disturbance flow in the surrounding liquid. The leading order and disturbance flow

have a total velocity potential of the form:

$$\Phi(r, \theta, t) = Q(t) \ln(r) + \sum_n d_n(t) r^{-n} \cos(n\theta). \tag{3.2}$$

The kinematic condition at the surface (2.1) at $O(a_n/R)$ determines the coefficients

$$d_n(t) = -\frac{R^{n+1}}{n} \left(\dot{b}_n + b_n \frac{\dot{R}}{R} \right). \tag{3.3}$$

Note that here, the azimuthal components u_θ and n_θ caused by the disturbance did not enter into the kinematic equation (2.1) because they are both of $O(b_n)$, thus making their product $O(b_n^2)$. Applying the Bernoulli integral (2.3), and the Laplace formula for the pressure jump across the surface, also to $O(b_n)$ yields the evolution equation for the mode amplitudes with coefficients which depend on the radial implosion dynamics:

$$\ddot{b}_n + \left(\frac{2\dot{R}}{R} \right) \dot{b}_n + \left(\frac{\ddot{R}}{R}(1 - n) \right) b_n = 0. \tag{3.4}$$

We can take advantage of the fact that we have a conserved energy to use (2.4) and (2.5) to rewrite $\dot{R}$ and $\ddot{R}$ in terms of E and R. This, along with using $\mathrm{d}/\mathrm{d}t = \dot{R}\,\mathrm{d}/\mathrm{d}R$ allows us to rewrite (3.4) so that the independent variable is R rather than t. Taking the limit that the implosion is inertially dominated and the radius has decreased far away from the system size R_∞, yields

$$b_n'' + \left(1 + \frac{1}{2\ln(\frac{R_\infty}{R})} \right) \frac{b_n'}{R} + (n - 1) \left(1 - \frac{1}{2\ln(\frac{R_\infty}{R})} \right) \frac{b_n}{R^2} = 0, \tag{3.5}$$

where $'$ denotes a derivative with respect to R.

Immediately we can clearly see the amplitude freezing and vibrational behavior

by taking the limit $\ln(R_\infty/R) \gg$ in (3.5), which corresponds to a radial implosion

follow $R = \alpha\tau^{1/2}$. Then, the governing equation takes the particularly simple equidi-

mensional form

$$b_n'' + \frac{b_n'}{R} + (n-1)\frac{b_n}{R^2} = 0, \tag{3.6}$$

with solutions for $b_n(R)$ of the form $b_n \propto R^{\pm i\sqrt{n-1}}$. These solutions neither grow

nor decay because the eigenvalues are entirely imaginary, but instead oscillate with

constant amplitude $b_{n,0}$ and an n-dependent frequency. The real part of the vibration

can be written

$$b_n(R) = b_{n,0}\cos(\sqrt{n-1}\ln R + \phi_{n,0}), \tag{3.7}$$

with $\phi_{n,0}$ an arbitrary phase shift defined by the initial conditions. The frequency

of the vibrations, $\sqrt{n-1}/R$ is n-dependent, with higher modes vibrating faster. All

the vibrations become faster and faster, or "chirp", as $R \to 0$ due to the divergent

$1/R$ dependence. This is a direct consequence of the singularity formation, where no

other length or time-scales other than the closure radius R and time τ are involved in

the dynamics. Thus, from simple scaling the frequency is forced to be proportional

to $1/R$.

To check that including the logarithmic corrections does not qualitatively change

the vibration freezing and chirping characteristics, we analyze (3.5) by introducing a

second slowly varying length scale defined as $y = \ln(R_\infty/R)$. Performing a standard

multiple scale analysis [34] we find that the modes are primarily oscillatory with am-

plitudes that grow extremely weakly and uniformly, as $(\ln(R_\infty/R))^{1/4}$. This growth

is shown in Fig. 3.1 and envelopes the numerical solutions to (3.4) for $n = 2$ and 5.

The growth can also be shown by transforming (3.5) into the y variable:

$$\frac{d^2 b_n}{dy^2} - \frac{1}{2y}\frac{db_n}{dy} + (n-1)\left(1 - \frac{1}{2y}\right)b_n = 0. \tag{3.8}$$
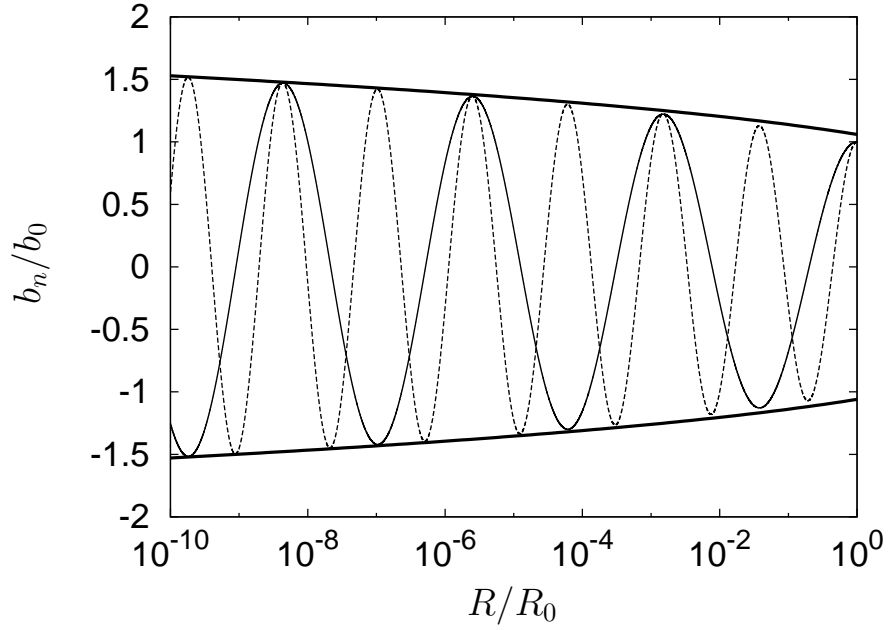
Figure 3.1: Numerical solutions to (3.4) for vibrational mode amplitudes in inertial limit, for modes $n = 2$ (dashed line), $n = 5$ (dotted line). The amplitudes grow weakly as the mean radius decreases, like $(\ln(R_\infty/R))^{1/4}$, predicted from solution to (3.5) using (thick solid line). Mode amplitudes are rescaled by their initial size b_0 and the mean radius R is rescaled by its initial size R_0, and $R_\infty/R_0 = 100$.

Solutions to (3.8) are of the form $b_n(y) = y^{3/2}e^{-i\sqrt{n-1}\,y}f(y)$ with $f(y)$ satisfying

$$2y\frac{\mathrm{d}^2 f}{\mathrm{d}y^2} + \frac{\mathrm{d}f}{\mathrm{d}y}(5 - 4i\sqrt{n-1}y) + f(1 - n - 5i\sqrt{n-1}) = 0. \tag{3.9}$$

Again transforming to the complex variable $z = 2i\sqrt{n-1}\,y$ we arrive at

$$z\frac{\mathrm{d}^2 f}{\mathrm{d}z^2} + \left(\frac{5}{2} - z\right)\frac{\mathrm{d}f}{\mathrm{d}z} - \left(\frac{5 - i\sqrt{n-1}}{4}\right)f = 0 \tag{3.10}$$

which is of the form of the confluent hyper-geometric differential (Kummer's) equation. The solution for $f(y)$ when $\mathrm{Re}(z) \gg 1$ (or $y \gg 1$, $R_\infty/R \gg 1$) decay like $f \propto z^{-5/4}$. Taken together with the above form for $b_n(y)$ yields a weak growth in the amplitude like $b_n(y) \propto y^{3/2-5/4} = y^{1/4}$ or $b_n(R) \propto (\ln(R_\infty/R))^{1/4}$.

The amplitude growth is so weak (in Fig. 3.1, increasing only by a factor of 1.5 as the mean radius deceases by 10 orders of magnitude) that the amplitudes are effectively constant. More importantly, because all modes grow within the same n-independent envelope, an initial mode distribution will still be preserved as the implosion proceeds. Numerical solutions to (3.5) for $n = 2$ and 5 are shown in Fig. 3.1. The weak growth follows the analytic prediction of $\ln(R_\infty/R)^{1/4}$.

Considering the vibrational modes relative to the leading-order radial implosion the shape becomes more distorted as R decreases to 0. Though the amplitudes are constant, the relative amplitudes b_n/R grow like $\tau^{-1/2}$, causing the shape to become increasingly more distorted. Taking the linear stability results to the point when $b_n = O(R)$ predicts the development of cusp-like structures on the interface. The shapes, especially when two or more modes are present can become quite complex as the vibrations occur with n-dependent frequencies. An illustration of shapes that occur as the void collapses for a combination of modes $n = 2$ and 3 is shown in
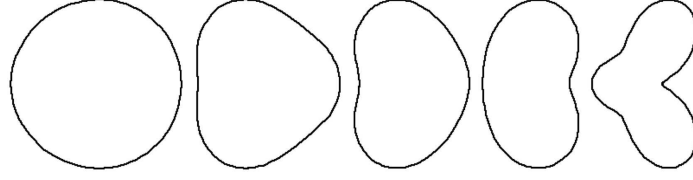
Figure 3.2: Illustration of void shapes for superposition of vibrational modes $n = 2$ and 3, with dynamics given by Eq. 3.7 in text. The shapes are rescaled by the mean radius which is collapsing to zero (left to right). As the mean radius collapses, the shapes become more distorted. Because the $n = 2$ and 3 modes are not vibrating in phase, complex shapes ensue.

Fig. 3.2.

At some point (once the mean radius R has collapsed to the size of the largest mode amplitude present) the approximation $b_n/R \ll 1$ breaks down and non-linear effects cannot be ignored. Recent numerical results utilizing a conformal mapping method have explored the non-linear regime that follows and found a rich landscape of different types of pinch-off depending sensitively on the initial conditions [35].

These vibrational modes are purely inertial, unlike most vibrations or waves on fluid interfaces. For example, a jet of water issued from an elliptic shaped nozzle will also undergo vibrations of the cross section shape, but this effect is due to a competition between inertia and surface tension [36]. The inertial shape vibrations here occur because once the flow and pressure fields are perturbed, there is no mechanism for the extra energy associated to be dissipated in this closed and conservative system. The extra energy could go into or out of the main radial implosion, but in this situation it remains in the perturbation leaving the radial dynamics unchanged.

To help visualize the dynamics of the inertial vibrations, we can track how the fluid moves in and out of the wells around the circle. The corresponding corrections to the pressure field and velocity field (after subtracting out the leading order radial implosion) can be calculated using the potential from (3.2) with the appropriate

coefficients from (3.3) given the evolution of the mode amplitude from (3.4). The disturbance pressure field $P(r, \theta)$ is found from evaluating the Bernoulli integral (2.3) at $O(b_n)$ and yields:

$$\delta P(r, \theta, t) = \frac{\rho \cos(n\theta)}{n} \left(\frac{R}{r}\right)^n \left(R\dot{s}_n + s_n \dot{R} \left(1 + n - nR^2/r^2\right)\right), \qquad (3.11)$$

where $s_n = \dot{b}_n + b_n \dot{R}/R$. The disturbance velocity field is $\vec{\nabla}\Phi$ at $O(b_n)$:

$$\delta \mathbf{u}(r, \theta, t) = \left(\dot{b}_n + b_n \frac{\dot{R}}{R}\right) \left(\frac{R}{r}\right)^{n+1} (\cos(n\theta)\, \hat{r} + \sin(n\theta)\, \hat{\theta}). \qquad (3.12)$$

For an $n = 4$ distortion the disturbance pressure and velocity fields are shown in Fig. 3. Physically, the pressure builds up in the wells, leading to a disturbance flow outwards towards the peaks. The pressure and velocity field oscillate, but are out of phase, so that as the shape rounds up to a circle, the pressure is uniform around the circle (in θ) but flow continues, and creates a well. The pressure in the well begins to build up again (lightest region in Fig. 3), and causes a reversal of flow out of the wells.

Thus far we have shown that when a small shape distortion is introduced, an imploding cylindrical void will undergo inertial shape vibrations about the radial implosion dynamics. Within the linear regime, these vibrations have constant amplitudes but grow relative to the shrinking mean radius. This scenario naturally provides an explanation for why experiments observe a wide variety of different disconnection events — the final moments at disconnection are sensitively linked to the earliest moments in the implosion process. Below we show that including additional physical effects into the model do not destroy this unique behavior within the experimental regime.
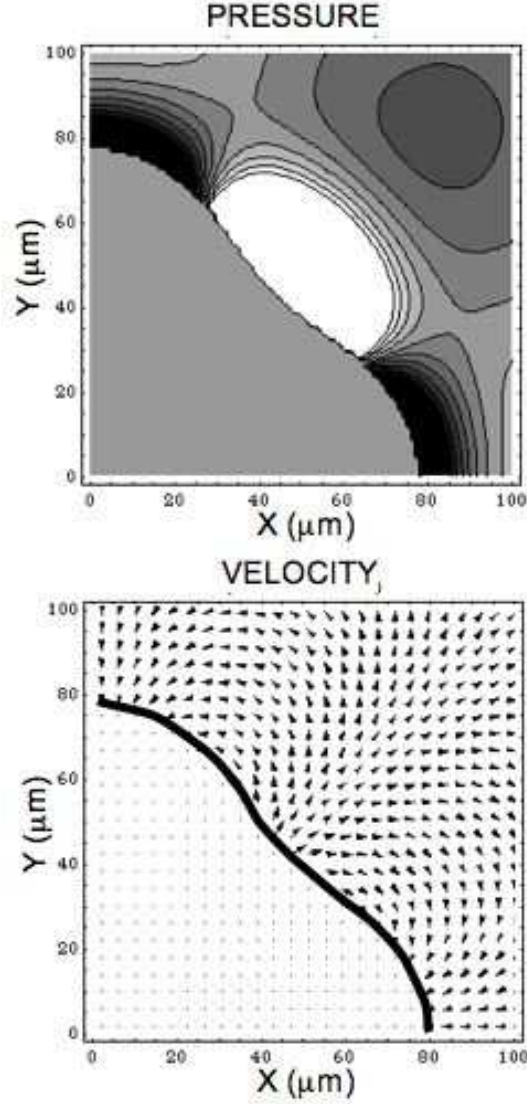
Figure 3.3: Example of disturbance to the pressure and velocity fields outside the surface due to an $n = 4$ shape distortion (one quadrant shown). For the pressure contours, inside the void the disturbance pressure is zero (medium grey) and outside the pressure has regions of positive (lighter) and negative (darker) pressure. The surface location is highlighted by the thick black line in the lower plot for the velocity. At this instant in time, the mean radius $R = 70\mu$m and has an implosion speed $\dot{R} = -0.7\mu$m/μs. For clarity, a large perturbation amplitude is shown with $b_4 = 8\mu$m and $\dot{b}_4 = -0.1\mu$m/μs.

CHAPTER 4

CONSEQUENCES OF ADDITIONAL PHYSICAL EFFECTS

The inertial shape vibrations were analyzed in a specialized limit of flow and fluid properties. It was assumed that the leading order dynamics was a purely radial implosion, that the liquid was completely inviscid, and was analyzed in the far asymptotic limit when the dynamics was completely inertially dominated. For the purely radial implosion in the inviscid liquid, the dynamics was shown to be integrable and evolve towards a singularity. Below we will test the consequences on the vibrational modes of destroying these two properties, in ways that are physically relevant.

This is done by first including viscous dissipation in the external liquid in the simplest manner possible, which destroys the integrability because the collapse energy is no longer conserved. Second, we remove the singularity by introducing a weak rotational flow into the external liquid which prevents the hole from collapsing to a point and forming a finite time singularity. Both of these effects are physically relevant as well – no experiment uses a perfectly inviscid liquid or can completely eliminate the presence of a weak swirling flow. We will find that within the experimental regime, the inertial shape vibration behavior described in the preceding section will be robust against these effects, for the small mode numbers (large wavelength disturbances) explored in the experiments. Finally, even though surface tension becomes irrelevant asymptotically, we account for capillary effects and find the vibration frequency is increased in the experimental regime before the vibrations settle in to their asymptotic behavior.

4.1 Viscous dissipation

To include viscous dissipation we must first consider the effect on the leading-order radial implosion dynamics, and then consequently the effect on the vibrational mode behavior. When viscous dissipation is included in the model, the implosion energy E is no longer strictly conserved and the leading-order symmetric collapse dynamics are no longer integrable and Hamiltonian. However, Eq. (2.4) still holds once the viscous contribution to the normal stress balance is taken into account. For the leading-order radial flow, viscous dissipation does not alter the form of the equations governing fluid flow but it does contribute to the normal stress balance on the surface: $p(R) = p_0 - \gamma\kappa + 2\mu\partial u_r/\partial r$, where μ is the liquid viscosity. Since $\partial u_r/\partial r = -\dot{R}/R$ on the surface, the governing equation (2.4) is then modified to

$$\Delta p + \frac{\gamma}{R} + 2\mu\frac{\dot{R}}{R} = \frac{\rho}{2}\dot{R}^2 - \rho(\dot{R}^2 + R\ddot{R})\ln(R_\infty/R). \tag{4.1}$$

Comparing the inertial and viscous terms we see that viscous dissipation will be relevant to the process when $\dot{R}R/\nu = Q/\nu = O(1)$ (with the kinematic viscosity $\nu = \mu/\rho$), i.e., when the dynamic Reynolds number is $O(1)$. If the implosion begins in an inertially dominated regime where $E \approx$ constant, this occurs very late in the implosion, at a length scale beyond the reach of a continuum theory, seen from $Q = \sqrt{E/\pi\rho\ln(R_\infty/R)}$. For the air cavity in water experiments the dynamic Reynolds numbers are typically on the order of $10^2 - 10^3$, which means that within the experimental regime, the radial collapse is inertially dominated and $E = $constant will produce the observed radial implosion dynamics.

Once we consider the shape perturbations, the velocity field is no longer purely radial, but has an azimuthal (θ) component. To fully include the effect of a small

viscosity in this problem would require a complete change in the solution method. The presence of viscosity means that vorticity can be generated and therefore the flow is no longer truly potential. However, if the vorticity is confined to a very shallow boundary layer near the surface where it is generated, we can again approximate the viscous effects as only contributing to the normal stress balance. Then, the stability analysis yields a revised equation for $b_n(t)$:

$$\ddot{b}_n \; + \; \left(\frac{2\dot{R}}{R} + 2\nu \frac{n(n+1)}{R^2} \right) \dot{b}_n$$
$$+ \; \left(\frac{\ddot{R}}{R}(1-n) + 2\nu \frac{n(n-1)\dot{R}}{R^3} \right) b_n = 0. \tag{4.2}$$

From (4.2) we can see that viscous effects can now play an earlier role for high mode numbers, because the viscous terms have prefactors $O(n^2)$ and will quickly begin to dominate. Figs. 4.1 and 4.2 plot results of numerical solutions to (4.2) for two values of dynamic Reynolds number, 10^2 and 10^3 (which over the range of the data change by only a factor of about 2). Figs. 4.1 and 4.2 (A) plot the vibration for a single mode $n = 2$, showing a decay in the amplitude relative to inviscid case (see Fig. 3.1), but the chirping behavior of the frequency is unchanged. In Figs. 4.1 and 4.2 (B), the envelopes for modes $n = 2 - 10$ are plotted, and clearly show the n-dependence of the rate of decay. All mode amplitudes experience decay due to viscous dissipation, but the short wavelength (high n) feel the strongest effect. The reason for the apparent amplitude growth in Fig. 4.1 B for $Q/\nu = 10^3$ is simply that the inertially dominated vibrations have weak growth (as in Fig. 3.1) which acts until viscous dissipation takes over as $R \to 0$. For the smaller $Q/\nu = 10^2$ in Fig. 4.2, the weak growth is completely washed out by a rapid decay in the amplitude.

To quantify the decay, we plot the spectrum of the mode amplitudes as a function

of mode number n at a given mean radius. We choose two values of the mean radius at which to evaluate the spectrum, $R/R_0 = 10^{-2}$ and 10^{-5} (so the mean radius collapses 2 or 5 decades from its initial value). The results are shown in Figs. 4.1 and 4.2 (C). The choice of the mean radius at which to evaluate the spectrum has no qualitative effect on the results. Both spectrums show rapid decay for high mode numbers, with more efficient decay for the lower dynamic Reynolds number set.

Overall, viscous dissipation does not effect the radial, symmetric implosion until exponentially small length-scales, but it has a dramatic effect on the vibrational mode behavior. The chirping characteristic of the vibrations persists, but the freezing of the mode amplitudes is lost and a rapid decay of the mode amplitudes occurs for high n and low dynamics Reynolds number.

To connect this result back to the experiments, we note that in the bubble breakup experiments, surface tension is effective in smoothing out the surface and removing any higher mode distortions which may be present, because the early dynamics is completely dominated by surface tension before the implosion begins [9, 10, 11]. But, if a short wavelength disturbance was present, viscous dissipation would be very efficient at wiping it out (Fig. 4.2). So in these experiments we expect only low mode number distortions to be present.

The solid body impact experiments do not have such a surface tension dominated regime and thus short wavelength disturbances may be present in the initial shape. With the faster radial implosion and higher dynamics Reynolds number in the experimental regime, viscous dissipation would cause decay of the highest modes but it is less effective here than in the bubble experiments so some higher modes could still be present, which could be part of the reason why the intricate textures and swarms of satellite bubbles are observed in those experiments [14].

(a) $n = 2$

(b) $n = 2 - 10$

(c) spectrum
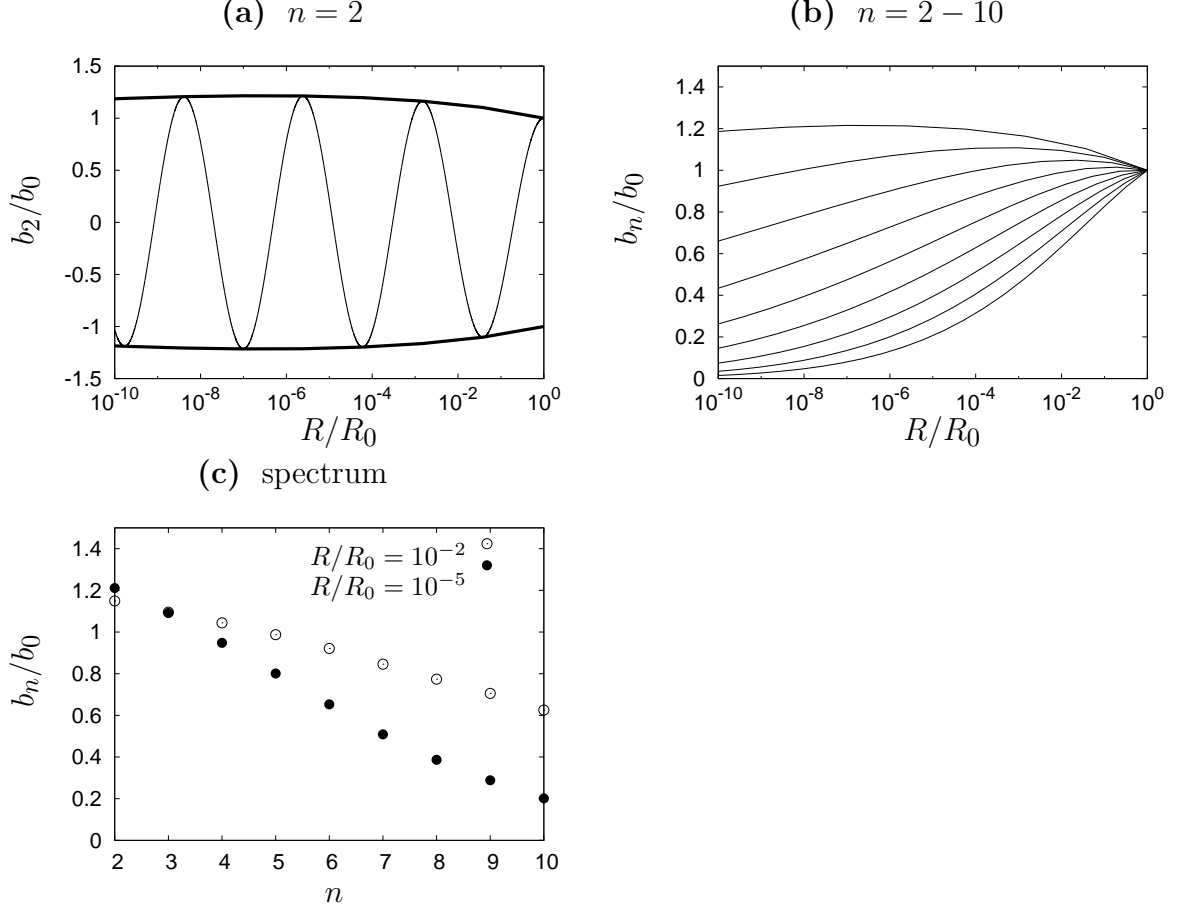
Figure 4.1: Amplitude decay due to viscous dissipation at the interface. Here, $R_\infty/R_0 = 10^2$ and the dynamic Reynolds number for the flow is $Q/\nu = 10^3$ when $R = R_0$. The amplitudes are rescaled by their initial values b_0 and the mean radius is rescaled by its initial value R_0. (a) Representative vibration for $n = 2$ (thin line) shows that viscous dissipation causes a decrease in the amplitude (envelope is thick line) and frequency of vibration. (b) Envelope of vibrational mode amplitudes for $n = 2 - 10$ (upper- to lower-most). Short wavelength (high n) disturbances are efficiently smoothed out by the presence of viscosity. (c) Amplitude spectrum taken at $R/R_0 = 10^{-2}$ (open circles) and at $R/R_0 = 10^{-5}$ (solid circles).

(a) $n = 2$

(b) $n = 2 - 10$

(c) spectrum
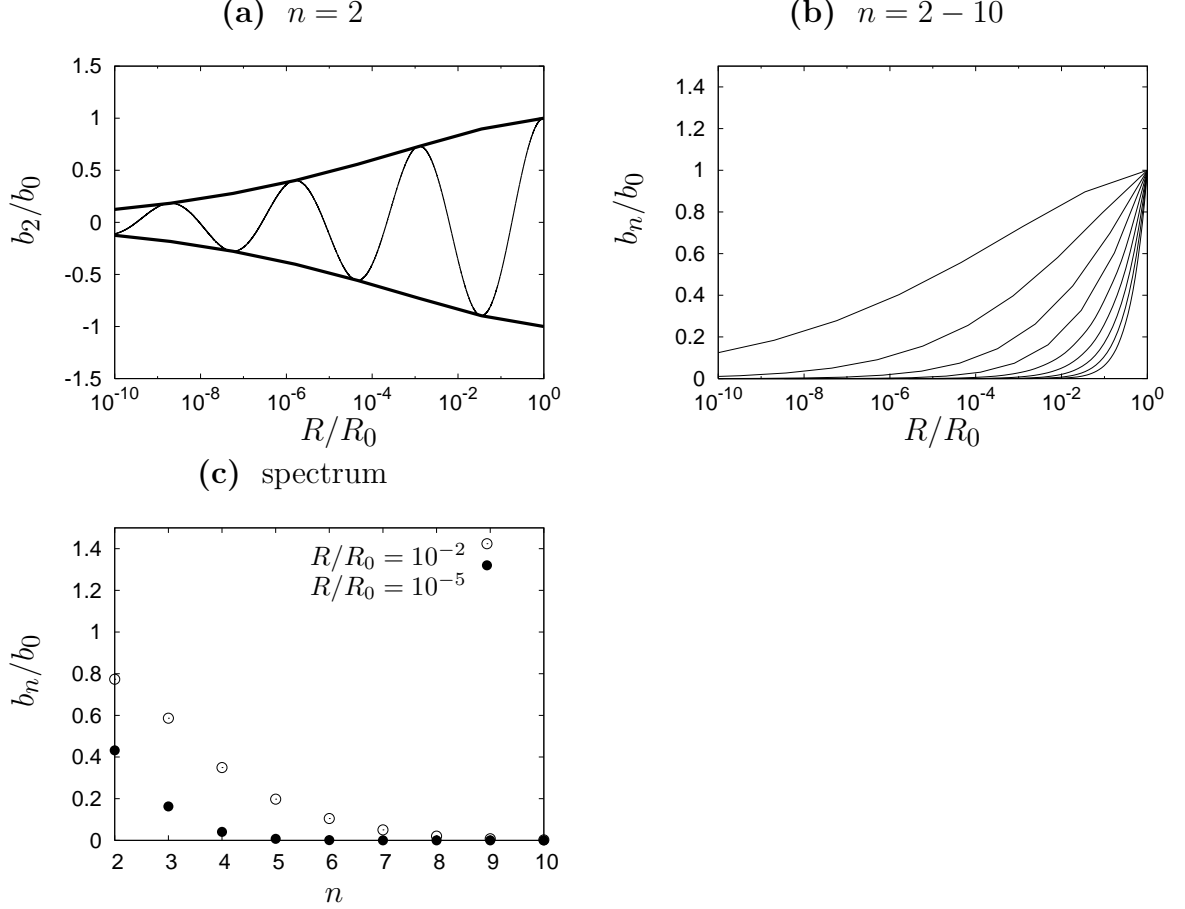
Figure 4.2: Amplitude decay due to viscous dissipation at the interface. Here, $R_\infty/R_0 = 10^2$ and the dynamic Reynolds number for the flow is $Q/\nu = 10^2$ when $R = R_0$. The amplitudes are rescaled by their initial values b_0 and the mean radius is rescaled by its initial value R_0. (a) Representative vibration for $n = 2$ (thin line) shows that viscous dissipation causes a decrease in the amplitude (envelope is thick line) and frequency of vibration. (b) Envelope of vibrational mode amplitudes for $n = 2 - 10$ (upper- to lower-most). Short wavelength (high n) disturbances are efficiently smoothed out by the presence of viscosity. (c) Amplitude spectrum taken at $R/R_0 = 10^{-2}$ (open circles) and at $R/R_0 = 10^{-5}$ (solid circles).

4.2   Rotational motion

Introducing a small rotational flow into the external liquid provides a clever way to remove the singularity formation that occurs as the radius of the void collapses to zero. This does not break the cylindrical symmetry, but causes the liquid to swirl around as the hole collapses. A consequence of the rotation is that finite amount of energy is always stored in the rotation flow because of angular momentum conservation, and a barrier or turning point in the radial motion is encountered (like in central force motion [37]) [38]. The turning point occurs at a non-zero but exponentially small radius (for a weak rotational flow), introducing an additional length- and time-scale to the implosion process. Thus, the rotational flow allows us to examine the consequences of the singularity formation (and decoupling of the implosion process from external scales) on the vibrational mode behavior.

For the axisymmetric, imploding cylinder, we now allow the liquid to be swirling inwards, possessing angular momentum. The velocity field then has an additional rotational component which can be written as $u_\theta = \Gamma/2\pi r$. Kelvin's circulation theorem states that the circulation Γ around a closed loop for potential flow is a constant,

$$\Gamma = \oint \mathbf{u} \cdot \mathbf{dl}, \tag{4.3}$$

determined by the initial conditions. Thus, the dynamics remains integrable with an additional conserved quantity, the circulation. The Hamiltonian in (2.5) must include the additional kinetic energy from the rotational flow. This energy is easily found by integrating u_θ over the liquid region and the total kinetic energy is now

$$E = \frac{M(R)}{2}\dot{R}^2 + \frac{M(R)}{2}\left(\frac{\Gamma}{2\pi R}\right)^2 \tag{4.4}$$

The evolution equation for $R(t)$ (2.4) is modified with an additional term on the right hand side, $\rho\Gamma^2/8\pi^2 R^2$.

The consequence of the rotation is that a singularity in the governing equations no longer occurs. Instead, a turning point in the motion occurs when $\dot{R} = 0$ which can be quickly seen from (4.4) to be exponentially small unless the rotational flow is large: $R_{turn}/R_\infty = \exp(-4\pi E/\rho\Gamma^2)$, where we have used the form for the mass from Chapter 2, $M(R) = 2\pi\rho R^2 \ln(R_\infty/R)$. This change occurs because the rotational flow contains a finite, and growing amount of energy as the hole collapses, preventing the radial velocity from diverging.

Upon again performing the linear stability analysis for the azimuthal shape perturbations, which now includes terms depend on the rotational flow u_θ, we find a description in terms of only the $\cos(n\theta)$ harmonics is insufficient to describe the dynamics. We must now include the second linearly independent $\sin(n\theta)$ harmonics and write the perturbed interface as: $S(\theta, t) = R(t) + \sum_n (b_n(t)\cos(n\theta) + c_n(t)\sin(n\theta))$. The vibrational modes b_n and c_n are coupled by their evolution equations:

$$\ddot{b}_n + \left(\frac{2\dot{R}}{R}\right)\dot{b}_n + (1-n)\left(\frac{\ddot{R}}{R} + n\left(\frac{\Gamma}{2\pi R^2}\right)^2\right)b_n + 2n\left(\frac{\Gamma}{2\pi R^2}\right)\dot{c}_n = 0, \qquad (4.5)$$

$$\ddot{c}_n + \left(\frac{2\dot{R}}{R}\right)\dot{c}_n + (1-n)\left(\frac{\ddot{R}}{R} + n\left(\frac{\Gamma}{2\pi R^2}\right)^2\right)c_n - 2n\left(\frac{\Gamma}{2\pi R^2}\right)\dot{b}_n = 0. \qquad (4.6)$$

For a weak ($\rho\Gamma^2/E \ll 1$) rotational flow the turning point occurs at an exponentially small radius, so the leading order radial implosion dynamics are unaffected until $R = O(R_{turn})$, outside the limits of a continuum theory. However, the vibrational mode behavior does experience a fundamental change – rather than forming standing waves with shapes that pulse as $R \to 0$, the rotational flow induces traveling waves around the circle, again with frequencies proportional to $1/R$. Numerical results for

b_n and c_n for $n = 10$ are shown in Fig. 4.3. The fast vibration is the original chirping described in Chapter 3 with frequencies $\sqrt{n-1}/R$, and the slower oscillation in the amplitude envelope is actually caused by the spinning of the quickly pulsing shapes as the hole closes.

To simply see this behavior in (4.5) and (4.6), assume the radial collapse dynamics follow $R = \alpha\tau^{1/2}$ and $u_\theta/u_r = \Gamma/\pi\alpha^2 \ll 1$. Then trying *a priori* solutions of the form $b_n = b_0 \cos(\omega_n \ln(R)) \cos(\sqrt{n-1}\ln(R))$ and $c_n = b_0 \sin(\omega_n \ln(R)) \cos(\sqrt{n-1}\ln(R))$ yields $\omega_n = \frac{n\Gamma}{\pi\alpha^2}$. The full shape can then be written (without the phases)

$$S(t,\theta) = R(t) + \sum_n b_{n,0} \cos[\omega_n \ln(R) - n\theta] \cos(\sqrt{n-1}\ln(R)), \qquad (4.7)$$

clearly showing the traveling wave nature of the solutions, with n-independent frequencies $(\omega_n/n)R^{-1} = (\Gamma/\pi\alpha^2)R^{-1}$. This is the frequency of the slow oscillations of the envelope of the the faster vibrations in Fig. 4.3. Even though the ratio $\Gamma/\pi\alpha^2$ is not perfectly constant as was assumed in the simple scenario above, but involves logarithmic corrections, it changes so slowly that it increased by only a factor of 3, over the 10 decades collapse of R. This is reflected in the visible weak variation of the long frequency.

Introduction of the weak rotational flow did not destroy the vibrational mode amplitude freezing behavior but did cause the emergence of another frequency in the dynamics, the n-independent frequency of the spinning motion of the shapes. The surface spins faster and faster as void closes, while the shapes vibrate with constant amplitude. The above analysis assumes the rotation is slower than the radial converging flow, and thus the effects of the finite turning radius turned out to be negligible. It would be interesting to fully examine the asymptotic behavior when the rotational flow becomes the same size as the radial flow, and then the destruction
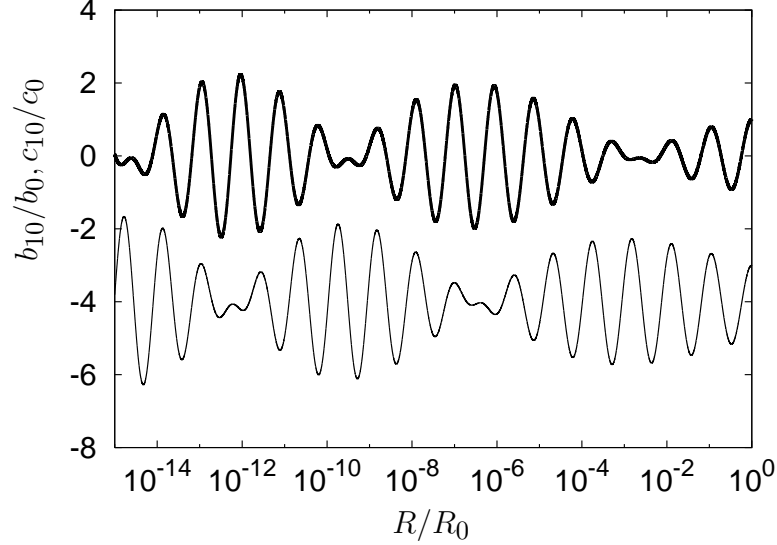
Figure 4.3: Coupled mode amplitudes with presence of swirl flow for $n = 10$, b_{10} (thick line) and c_{10} (thin line, displaced downwards for clarity). The initial conditions at $R = R_0$ are $b_{10} = c_{10} = b_0$ with zero derivative. The relative swirl flow strength is $u_\theta/u_r \approx 10^{-2}$ (over the range of the plot it increases only to $3 \cdot 10^{-2}$ as R decreases). $R_\infty/R_0 = 10^2$ and the implosion energy is about

of the singularity formation would likely cause rapid amplitude growth or decay.

In the bubble experiments which start with a quiescent liquid bath, there is likely very little circulation present, though it is not possible to completely eliminate. In this case, the presence of a weak and unintentional rotational flow are not damaging to the vibrational mode behavior, but simply cause a slow spinning of the vibrating shapes. Such a rotational flow could be the cause behind observations of rotating surfaces and satellite bubbles [39, 40].

4.3   Surface tension

Surface tension forces become negligible to the radial implosion in the asymptotic inertially dominated regime as seen in (2.5) and verified by experimental measurements

of the implosion dynamics. However, here we will see that the effect of surface tension on the inertial vibrations within the experimental regime, is to cause a short-lived but rapid growth in mode amplitude and increase in frequency in the experimental regime before converging onto the asymptotic form given in (3.4). We modify (3.4) so that the local curvature is no longer simply $1/R$ but to first order in b_n/R: $\kappa \approx \frac{1}{R} + (n^2 - 1)b_n \cos(n\theta)/R^2$, yielding

$$\ddot{b}_n + \left(\frac{2\dot{R}}{R}\right)\dot{b}_n + \left(\frac{\ddot{R}}{R}(1 - n) + \frac{\gamma n(n^2 - 1)}{\rho R^3}\right)b_n = 0. \tag{4.8}$$

This adjusts the local Laplace pressure jump as we go around the shape through the peaks and valleys. When the radial dynamics is inertially dominated, the b_n coefficient in (3.5) now includes $\gamma n(n + 1)\pi R \ln(R_\infty/R)/E$. By comparison of the original inertial term in this coefficient, we see that the cutoff for when surface tension will no longer affect the vibrations is when $R < R_n^{crit}$ with the critical radius

$$R_n^{crit} \ln(R_\infty/R_n^{crit}) = \frac{E}{\gamma \pi n(n + 1)}. \tag{4.9}$$

We numerically integrate the solutions for $b_n(t)$ using the radial dynamics from a numerical solution of (2.7). The solutions show that the effect of surface tension is to speed up the vibrations and give additional short-lived amplitude growth when the mean radius is large (see Fig. 4.4). Fig. 4.4 (A) shows the growth and frequency increase for an $n = 10$ vibration. The amplitude envelopes for $n = 2 - 30$ are plotted in Fig. 4.4 (B), and the spectrum (using the same definition for the case of viscous dissipation above) in (C). Higher modes are impacted more severely and for longer into the implosion, since the critical radius R_{crit} decreases with increasing n.

The bubble pinch-off experiments are unique in the fact that they are initially

dominated by surface tension (which will efficiently smooth out high modes), but by the time the mean radius reaches $O(300\mu\text{m})$ the radial implosion is inertial. This gives surface tension a short time to act on the vibrational modes before the inertial limit is reached for $R < R_n^{crit}$.

(a) $n = 10$

(b) $n = 2 - 30$

(c) spectrum
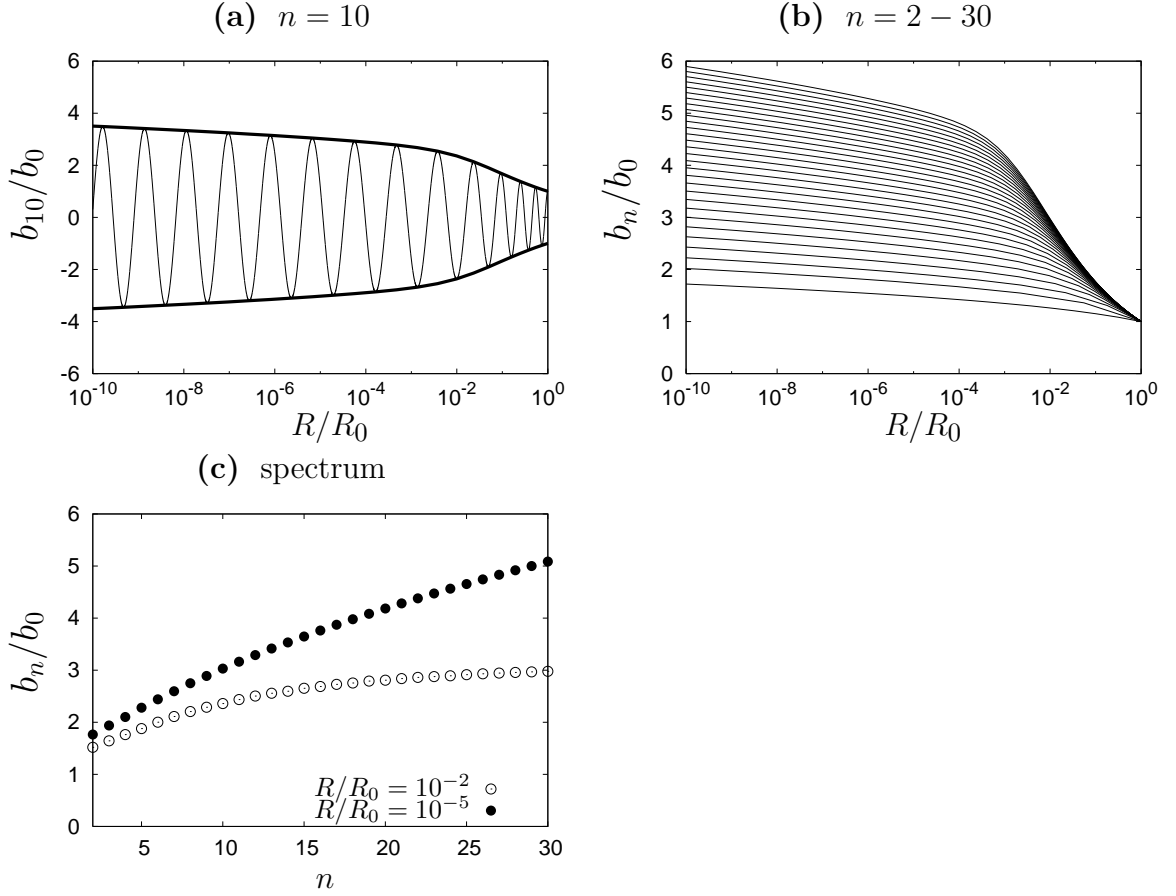
$R/R_0 = 10^{-2}$ ○
$R/R_0 = 10^{-5}$ ●

Figure 4.4: Effect of surface tension on early (large R) vibrational mode behavior. Here, $R_\infty/R_0 = 10$ and $E/\pi\gamma R_0 = 10$. The amplitudes are rescaled by their initial values b_0 and the mean radius is rescaled by its initial value R_0. (a) Representative vibration for $n = 10$ (thin line) shows that surface tension causes an initial increase in the amplitude (envelope is thick line) and frequency of vibration. After the mean radius has decreased beyond $R_{10}^{crit} \approx R_0/10^2$, the vibration settles in to the asymptotic inertial state with amplitudes and periods as in Fig. 3.1. (b) Envelope of vibrational mode amplitudes for $n = 2 - 30$ (lower- to upper-most). (c) Amplitude spectrum taken at $R/R_0 = 10^{-2}$ (open circles) and at $R/R_0 = 10^{-5}$ (solid circles).

CHAPTER 5

CONNECTION BETWEEN THEORY AND
EXPERIMENTS

The preceding chapters laid out a scenario of how and why a nearly cylindrical void collapsing in an inviscid liquid retains an imprint of initial distortions to its shape. The cylindrically-symmetric model of Chapter 2 predicted how the void radius should collapse to a point, and the stability analysis of Chapter 3 predicted that and initial distortion causes vibrations of the shape as the implosion proceeds. The vibration amplitudes of all wavelength disturbances become frozen, and eventually overtake the leading-order symmetric implosion, generating strong distortions. Consideration of viscous dissipation, rotational flow, and surface tension effects in Chapter 4 predicts that the mode amplitude freezing and chirping (frequencies $\propto 1/\tau$) are characteristics within the realm of experimental observation.

Below we briefly review two types of experiments that generate void collapse in water. Then, because the vibrational behavior is inherently linked to the radial implosion dynamics via (3.4) we show the quasi-2D is capable of describing the evolution of 3D experimental profiles. Finally, we directly compare an experimentally observed shape vibration to the prediction of (3.4) for an $n = 2$ vibrational mode.

5.1   Review of experiments

In the bubble release experiments a bubble is grown quasi-statically by slowly pumping gas through a nozzle [9, 10, 11]. Surface tension keeps the bubbles connected to the nozzle until it can no longer stabilize the surface against the upwards pull of buoyancy. At this point, the neck of the bubble rapidly pinches off. The entire dis-

connection process occurs on a ms time scale, much faster than the rising motion of the bubble. The earliest dynamics are determined by a competition between surface tension and gravity. However, once the implosion begins, the inertia of the water rushing in to fill the void quickly starts to dominate the process, evidenced by the time evolution of the minimum radius h_{min} following close to a 1/2 power law in time, rather than 2/3 if surface tension were to drive the flow.

For the disc impact experiments, a solid disc is rapidly drawn into a bath of water, creating a cavity in its path [14, 12, 16]. Because of the high impact velocities used, the initial Weber number, which characterizes inertial effects relative to surface tension is greater than 10^2 ($We = \rho U^2 h/\gamma$; ρ is the liquid density, γ is the surface tension of the gas/liquid interface, U a characteristic velocity scale, h a characteristic length scale). Thus there is no regime here where surface tension can efficiently act to smooth out distortions to the cavity shape.

Both types of experiments observe a medley of different kinds of disconnection events depending on the specifics of the set-up, geometry and orientation of the nozzle or disc, and control parameters. In the bubble experiments, side-by-side satellite bubbles remain after disconnection if the nozzle is not carefully leveled [9, 10]. Fig. 1.1 (C) shows the bubble neck before and after disconnection when the nozzle has been purposely tilted by $2°$. Even more exotic and highly asymmetric shapes are observed if the bubble is not grown quasi-statically from the circular nozzle, but is instead blown rapidly through a slot shaped nozzle [10]. Often times in the impact experiments, the surface before disconnection appears textured, and after disconnection leaves behind a disordered swarm of satellite bubbles,rather than cleanly disconnecting at a point [14, 12]. These observations signal an instability in the underlying dynamics to azimuthal and/or axial perturbations, which prevents the axisymmetric implosion from being realized under generic conditions. Similar effects have not been observed in

experiments where surface tension is the force driving breakup. For example, a water drop breaking in air appears to always break in a universal way, independent of the exact experimental set-up [18]. Despite the clear evidence for the initial distortions in the azimuthal direction playing a critical role in the dynamics before and after bubble disconnection, it remained unexplored in the context of cylindrical voids until recently [13]. The accumulation of experimental results suggests that the fixed point for axisymmetric cavity collapse proposed [8] is not stable once the azimuthal direction is considered.

The final stages of both implosion situations have the same inertia- dominated dynamics, but the initial states are quite different. The impact experiments never pass through a surface tension dominated regime, whereas the bubble experiments always start there. This puts both experiments in unique positions. For impact, large amplitude and/or short wavelength distortions can be applied by using different shaped discs, because surface tension will not smooth them out. However, the advantage in the bubble experiments is the possibility to generate smooth, low wavelength, single mode perturbations to the shape.

5.2   Axisymmetric implosions

With the implosion dynamics outlined above we can now compare the profiles predicted by conservation of energy to those actually observed in experiments. Neck profiles from traces of experimental images of a bubble released from a 4 mm diameter circular nozzle are shown in Fig. 5.1 (b). To generate the theoretical profiles for comparison we first use the time-dependence of the minimum (at $z = 0$) to define the implosion energy per unit length. Within the range shown, the radius is following close to a 1/2 power law, signaling that the radial implosion is now far within the
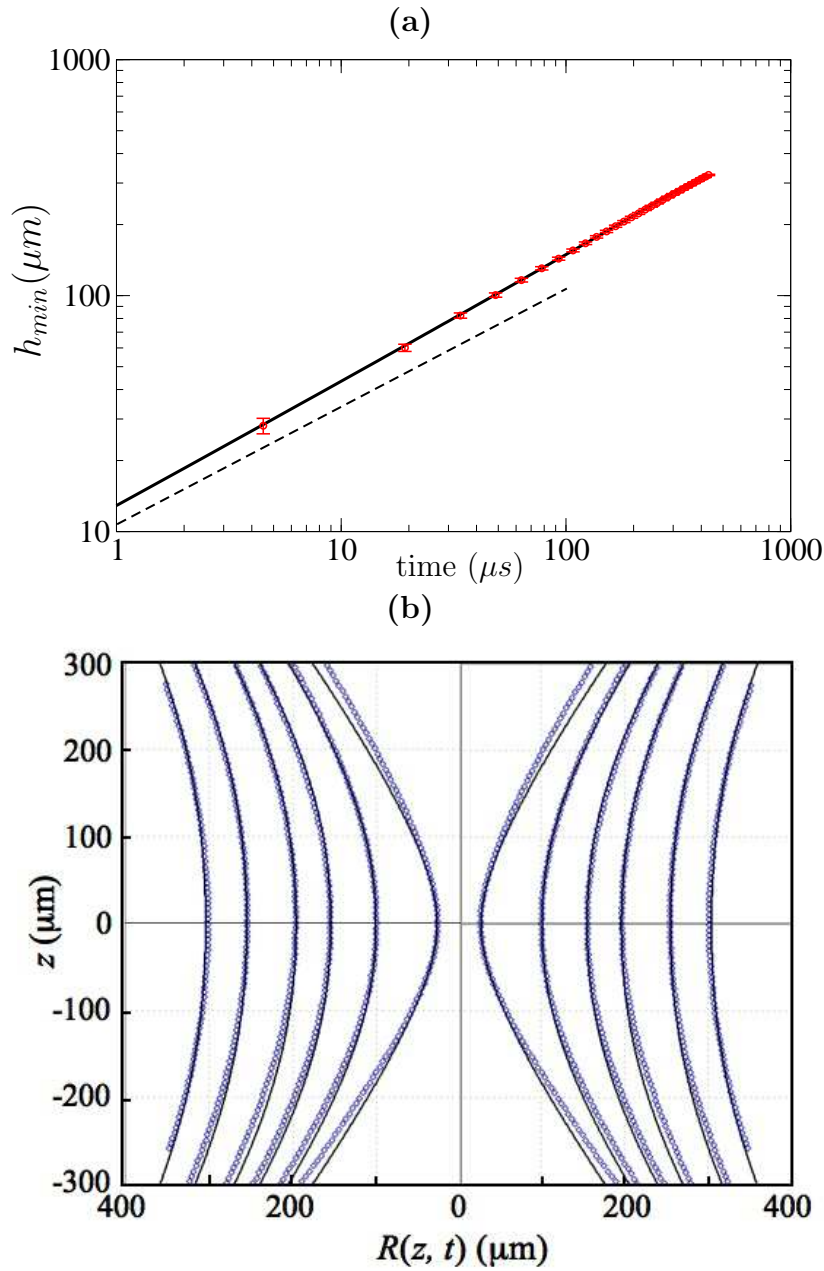
Figure 5.1: (a) Collapse of minimum radius for air bubble released from circular, 4mm diameter nozzle (red circles). Theoretical inertial implosion from (2.7) with an implosion energy per unit length of $E = 12$ dyne (black line). Dashed line shows slope of 1/2. (b) Experimental neck profiles of the same air bubble (blue diamonds). Theoretical profiles calculated as described in text using conservation of energy for each isolated layer (lines). Profiles are at 4.5, 49, 108, 166, 270, and 372 μs before disconnection (inner to outer curves). Experimental data provided by Nathan Keim (U. of Chicago).

inertially dominated regime. We then compare the evolution of the minimum to that predicted in the inertial regime, from numerical integration of (2.7) to determine the implosion energy E.

Taking $R_\infty = 2$mm, a physically relevant length scale as it is the radius of the nozzle, we find $E = 12$ dyne gives the best fit to the minimum (Fig. 5.1 (a)). The result is insensitive to the value of R_∞ used and good fits within experimental error can be found for $R_\infty = 1$mm with $E = 8.7$ dyne or up to $R_\infty = 4$mm with $E = 15$ dyne. These results would be indistinguishable by eye compared to those shown in Fig. 5.1 (a).

The implosion energy of 12 dyne was then applied at every height to track the full profile evolution. Because of the time invariance in the problem, the symmetric form of the profile closest to disconnection (innermost profile, averaged about $z = 0$) was used as the initial state, and then the expansion of the radius at each height was evolved according to $\dot{R} = +\sqrt{E/\pi\rho R^2 \ln(R_\infty/R)}$. Though the angles observed in bubble experiments typically are not small (half angles range from about 25-35 degrees depending on conditions), the quasi-2D model does a surprisingly good job describing the complete 3D surface evolution. This suggests the errors involved in applying the quasi-2D model are quite small over the finite range in h_{min} afforded by the experiment, though this remains to be checked via numerical simulation.

One aspect of the experiments which is quite obviously not captured in the model is the development of an up/down asymmetry in the cones above and below the minimum. The upper cone has an opening angle which is larger than the lower by about 5 degrees, but the precise amount depends on the vertical range used to define the angle. One might think that this could be simply accounted for within the framework of the 2D model by incorporation of a hydrostatic pressure gradient, which would break the axial symmetry about the minimum.

To introduce the hydrostatic pressure gradient $-\Delta\rho g$ we simply include it in the Hamiltonian (2.5) so the pressure term becomes $(\Delta P - \Delta\rho g z)\pi R^2$. Then, the energy is a function of z, with deeper layers having larger potential energies because the hydrostatic pressure at $r = R_\infty$ is higher there. If the radius at the same height above and below $z = 0$ are equal, the one with higher energy has a faster implosion rate (2.7). Thus, naïvely, one might expect that the cone below the origin will implode faster and have a smaller angle relative to the upper cone. However, one finds that this is not the case. Instead of causing a change in the cone angles, the primary effect is a downwards linear translation of the profile with the angles unaffected.

The profiles can be shifted to follow this translation of the minimum and are of the form $R(\psi)^2 = h_{min}^2 + 2c_0 H_0 \psi^2 + c_2 \psi^4$ where h_{min} is the radius of the minimum at $z = z_{min}$ and $\psi = z - z_{min}$. The cone angles remain $\sqrt{2c_0 H_0}$. The only possibility for the observed difference in apparent cone angles is if the ψ^3 term is very large, which requires the hydrostatic energy to be a substantial component of the implosion energy. This case is relevant to the larger-scale impact experiments [12, 14] but not for bubble pinch-off where the scale of the neck is $O(100\mu\text{m})$. An additional inconsistency is fact that if the difference in cone angles was caused by a large hydrostatic pressure gradient, the motion of the minimum would be downwards, but the experiments observe and the upwards motion of the minimum. Within the framework above, the hydrostatic pressure alone is not sufficient to explain the difference in cone angles and upwards motion of the minimum observed in the experiments. The up/down asymmetry which appears may be partly due to the slow upwards motion of the buoyant bubble, but is likely related to non-local flow coupling or energy transfer in the vertical direction, and is a point to be examined further in the future.

5.3 Predicted and observed vibrational mode

Recent experiments at the University of Chicago have been able to observe vibrations of the bubble neck shape as it implodes by releasing a bubble from an oblong nozzle [13, 39]. As the bubble grows from the nozzle, the neck is initially elongated in the same direction as the slot. Though surface tension is efficient in rounding up the bubble neck, it does not completely erase the effect of the highly asymmetric nozzle, and a small asymmetry in the cross section can be seen.

As the neck begins to rapidly implode, the neck shape vibrates so that at a later time it will be elongated in a direction opposite to slot. Depending on the speed at which the bubble is released from the slot nozzle (either quasi-statically or via a rapid burst of air) different numbers of periods can be observed. Fig. 5.2 shows these vibrations for quasi-static release from a slot of size 1.6 mm by 9.6 mm. By recording the implosion with two high speed cameras at a 90 degree angle, the perturbation amplitude is simply the half the difference in the measured widths from the two views $a_2 = (h_{side} - h_{front})/2$, and the mean radius is $\bar{R} = (h_{side} + h_{front})/2$.

Above a measured mean radius of $\bar{R} \approx 400\mu$m there is a rapid decay of the distortion amplitude which is likely due to the fact that the dynamics is truly three-dimensional and dominated by surface tension in this regime. Around $\bar{R} \approx 300\mu$m a vibration centered around $a_2 = 0$ sets in and continues until the last possible data point when $\bar{R} \approx 20\mu$m. Below $\bar{R} \approx 10\mu$m there is evidence of some weak decay in the amplitude, which could be due to viscous dissipation. Though the vibration shown in Fig. 5.2 is at height of the minimum radius in the experiment, it is also possible to observe the vibrations vibrations at different heights along z.

Below we outline the parameters, which are consistent with the experiment, used in the model to generate the theoretical vibration shown in Fig. 5.2. We begin by
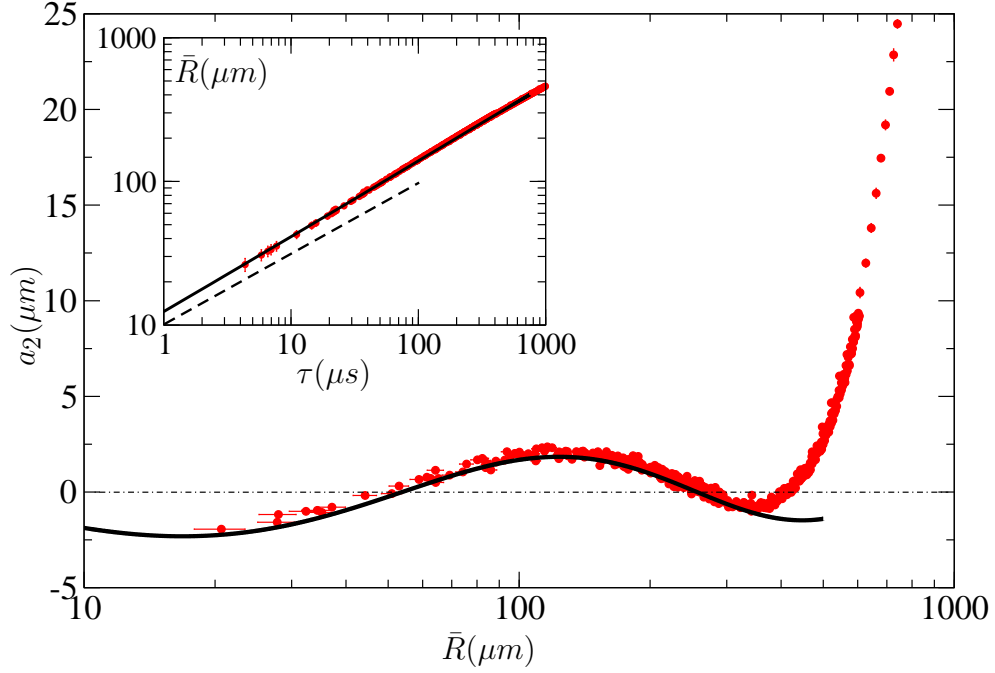
Figure 5.2: Experimentally observed vibrations of $n = 2$ mode by release from 1.6 mm by 9.6 mm slot nozzle (red). Theoretical vibration calculated from (4.8) as described in text (solid black line). Inset: Experimental mean radius collapse (red) corresponds to an inertial implosion with $E = 12$ dyne, and $R_\infty = 5mm$ (solid black). A power-law of $1/2$ is shown by the dashed line for comparison.

defining the total energy of the symmetric radial collapse which reproduces the radial inertial implosion dynamics for $\bar{R}(t)$. For the data shown in the inset to Fig. 5.2, this value is $E = 12$ dyne/cm when $R_\infty = 5$mm, the average radius of the slot. Similarly to the data in Fig. 5.1, while R_∞ is chosen within a physically meaningful range as the system size, the radial dynamics from energy conservation (2.7) describe the observed trajectory. Below we estimate the appropriate value for γ to be used in the evolution equation for $a_2(t)$ (4.8) which will take into account the axial curvature contribution to the Laplace pressure jump across the interface as done in (2.16).

From examination of experimental images of the data set used to generate the data shown in Fig. 5.2 we find that $R_{ax}/h_{min} \approx 2.8$. The value of 2.8 was chosen

by taking the average of the ratio R_{ax}/h_{min} over the range of the experimentally observed vibration. Thus, to effectively include the axial contribution, a value of $\gamma = (1 - 1/2.8)\gamma_0 = 0.64\gamma_0 = 46$ dyne/cm where γ_0 is the surface tension of an air water interface at room temperature, 72 dyne/cm, was used in the numerical solution of (4.8). The black line plotted in Fig. 5.2 is the result of a numerical solution to (4.8) with the parameters outlined above. The amplitude and phase (not predictable in this model) were chosen to fit the peak around $\bar{R} = 100\mu$m.

CHAPTER 6

CONCLUSION

The 2D model of the implosion of a cylindrical void in water is an integrable Hamiltonian system with special properties. These properties include conservation of the implosion energy and an exceptional perturbation mode spectrum which freezes as the implosion proceeds, and causes constant amplitude inertial vibrations about the radial implosion. This ideal system is closely related to the dynamics of the thin neck of air which collapses as an air bubble disconnects from an underwater nozzle. The memory mechanism in the simplified model is capable of explaining why asymmetries are observed to persist in experiments, and has predictive power for how azimuthal disturbances on the surface can dramatically alter the final stage of the pinch-off process.

The main features (amplitude freezing and vibrational chirping) of the inertial vibrations are robust against additional effects of surface tension, viscous dissipation, and rotational flow within the experimental regime, and thus we are able to directly compare the predicted vibrational mode to one excited in experiments. However, when comparing the observed amplitude and frequency of the $n = 2$ vibration, the most important effect was found to be surface tension. Inclusion of surface tension effects via the Laplace pressure jump across the interface acted to speed up the vibrations for a short time within the experimental regime.

At this point, a variety of physical effects were considered separately, to isolate the individual consequences on the vibrational mode spectrum. There is the potential for interesting mode spectrums to arise if multiple effects are combined. For example, the form of the normal stress balance on the interface will change substantially if both viscous dissipation and a rotational flow are included. It may also be possible

to find peaks in the spectrum, where one wavelength grows more rapidly than others, when combining surface tension (which causes amplitude growth) with viscous dissipation (which causes amplitude decay). More exploration of the outcome of these possibilities will be necessary to predict vibrational mode behavior for a larger range of experimental parameters.

REFERENCES

[1] Stone, H. A. Dynamics of drop deformation and breakup in viscous fluids. *Ann. Rev. Fluid Mech.* **26**, 65 (1994).

[2] Eggers, J. Nonlinear dynamics and breakup of free-surface flows. *Rev. Mod. Phys.* **69**, 865 (1997).

[3] Pumir, A. & Siggia, E. D. Finite-time singularities in the axisymmetric three-dimensional euler equations. *Phys. Rev. Lett.* **68**, 1511–1514 (1992).

[4] Barenblatt, G. I. *Scaling, self-similarity and intermediate asymptotics* (Cambridge University Press, Cambridge, UK, 1996).

[5] Kadanoff, L. P. Singularities and blowups. *Phys. Today* **50**, 11 (1997).

[6] Day, R. F., Hinch, E. J. & Lister, J. R. Self-similar capillary pinch-off of an inviscid fluid. *Phys. Rev. Lett.* **80**, 704–707 (1998).

[7] Leppinen, D. & Lister, J. R. Capillary pinch-off in inviscid fluids. *Phys. Fluids* **15**, 568–578 (2003).

[8] Eggers, J., Fontelos, M. A., Leppinen, D. & Snoeijer, J. H. Theory of the collapsing axisymmetric cavity. *Phys. Rev. Lett.* **98**, 094502 (2007).

[9] Burton, J. C., Waldrep, R. & Taborek, P. Scaling and instabilities in bubble pinch-off. *Phys. Rev. Lett.* **94**, 184502 (2005).

[10] Keim, N. C., Moller, P., Zhang, W. W. & Nagel, S. R. Breakup of air bubbles in water: Memory and breakdown of cylindrical symmetry. *Phys. Rev. Lett.* **97**, 145503 (2006).

[11] Thoroddsen, S. T., Etoh, T. G. & Takehara, K. Experiments on bubble pinch-off. *Phys. Fluids* **19**, 042101 (2007).

[12] Duclaux, V. *et al.* Dynamics of transient cavities. *J. Fluid Mech.* **591**, 1–19 (2007).

[13] Schmidt, L. E., Keim, N. C., Zhang, W. W. & Nagel, S. R. Memory encoding vibrations in a disconnecting air bubble. *Nature Physics* (2009). Advance online publication, 06 April 2009 (doi:10.1038/nphys1233).

[14] Bergmann, R. *et al.* Giant bubble pinch-off. *Phys. Rev. Lett.* **96**, 154505 (2006).

[15] Gekle, S., van der Bos, A., Bergmann, R., van der Meer, D. & Lohse, D. Non-continuous froude number scaling for the closure depth of a cylindrical cavity. *Phys. Rev. Lett.* **100**, 084502 (2008).

[16] Bergmann, R., van der Meer, D., Gekle, S., van der Bos, A. & Lohse, D. Controlled impact of a disk on a water surface: Cavity dynamics. Preprint, to appear in J. Fluid Mech.

[17] Gordillo, J. M., Sevilla, A. & Martínez-Bazán, C. Bubbling in a co-flow at high reynolds number. *Phys. Fluids* **19**, 077102 (2007).

[18] Shi, X. D., Brenner, M. P. & Nagel, S. R. A cascade of structure in a drop falling from a faucet. *Science* **265**, 219–222 (1994).

[19] Chen, Y. C. & Steen, P. H. Dynamics of inviscid capillary breakup: collapse and pinchoff of a film bridge. *J. Fluid Mech.* **341**, 245–267 (1997).

[20] Ott, E. *Chaos in Dynamical Systems* (Cambridge University Press, Cambridge, U. K., 2002).

[21] Besant, W. H. *Hydrostatics and Hydrodynamics* (Cambridge University Press, 1859).

[22] Rayleigh, L. On the pressure developed in a liquid during the collapse of a spherical cavity. *Phil. Mag.* **34**, 94 (1917).

[23] Landau, L. D. & Lifshitz, E. M. *Fluid Mechanics: Course of Theoretical Physics, Vol. 6* (Pergamon Press, Oxford, UK, 1987).

[24] Plesset, M. S. & Prosperetti, A. Bubble dynamics and cavitation. *Ann. Rev. Fluid Mech.* **9**, 145–185 (1977).

[25] Hilgenfeldt, S., Lohse, D. & Brenner, M. Phase diagrams for sonoluminescence. *Phys. Fluids* **8**, 2808 (1996).

[26] Longuet-Higgins, M. S., Kerman, B. R. & Lunde, K. The release of air bubbles from an underwater nozzle. *J. Fluid Mech.* **230**, 365 (1991).

[27] Oguz, H. N. & Prosperetti, A. Dynamics of bubble growth and detachment from a needle. *J. Fluid Mech.* **257**, 111 (1993).

[28] Lohse, D. *et al.* Impact on soft sand: Void collapse and jet formation. *Phys. Rev. Lett.* **93**, 198003 (2004).

[29] Gordillo, J. M., Sevilla, A., Rodríguez-Rodríguez, J. & Martínez-Bazán, C. Axisymmetric bubble pinch-off at high reynolds numbers. *Phys. Rev. Lett.* **95**, 194501 (2005).

[30] Percival, I. C. & Richards, D. *Introduction to Dynamics* (Cambridge University Press, Cambridge, 1983).

[31] Zakharov, V. E. Stability of periodic waves of finite amplitude on surface of a deep fluid. *J. Prikl. Mekh. Tekhn. Fiziki.* **9**, 86–94 (1968).

[32] Whitham, G. B. A new approach to problems of shock dynamics. part 1. two-dimensional problems. *J. Fluid Mech.* **2**, 145–171 (1957).

[33] Evans, A. K. Instability of converging shock waves and sonoluminescence. *Phys. Rev. E* **54**, 5004–5011 (1996).

[34] Bender, C. M. & Orzag, S. A. *Advanced Mathematical Methods for Scientists and Engineers (International Series in Pure and Applied Mathematics* (Mcgraw-Hill College, 1978).

[35] Lai, L., Turitsyn, K. & Zhang, W. W. Asymmetric bubble disconnection: persistent vibration evolves into smooth contact. To be published.

[36] Rayleigh, J. W. S. On the capillary phenomena of jets. *Proc. R. Soc. London Ser. A.* **29**, 71–97 (1879).

[37] Landau, L. D. & Lifshitz, E. M. *Mechanics: Course of Theoretical Physics, Vol. 1* (Pergamon Press, Oxford, UK, 1976).

[38] Rogers, J. C. W. & Szymczak, W. G. Computations of violent surface motions: Comparisons with theory and experiment. *Phil. Trans. R. Soc. Lond. A* **355**, 649–663 (1997).

[39] Keim, N. C. Unpublished experimental data.

[40] Thoroddsen, S. T., Etoh, T. G. & Takehara, K. High-speed imaging of drops and bubbles. *Annu. Rev. Fluid Mech.* **40**, 257–285 (2008). Online Supplementary Movies.